

1 **In situ characterization of nanoscale strains in loaded whole joints via synchrotron X-ray**  
2 **tomography**

3  
4 Madi K<sup>1,2#</sup>, Staines KA<sup>3#</sup>, Bay BK<sup>4\*</sup>, Javaheri B<sup>5</sup>, Geng, H<sup>1,6</sup>, Bodey AJ<sup>7</sup>, Cartmell S<sup>6</sup>,  
5 Pitsillides AA<sup>5\*</sup>, Lee PD<sup>1,8\*</sup>

6  
7 # Joint first authorship: Madi, Staines, \* Joint senior and corresponding authors: Lee,  
8 Pitsillides, Bay

9 <sup>1</sup> Research Complex at Harwell, RAL, Didcot, OX11 0FA, UK

10 <sup>2</sup> 3Dmagination Ltd, Fermi Avenue, Harwell Oxford, Didcot, OX11 0QR, UK

11 <sup>3</sup> School of Applied Sciences, Edinburgh Napier University, Edinburgh, EH11 4BN, UK

12 <sup>4</sup> College of Engineering, Oregon State University, Corvallis, OR, 97331, USA

13 <sup>5</sup> Comparative Biomedical Sciences, Royal Veterinary College, Royal College Street,  
14 London, NW10TU, UK

15 <sup>6</sup> Department of Materials, The University of Manchester, Manchester, M13 9PL, UK

16 <sup>7</sup> Diamond Light Source, Harwell Science & Innovation Campus, Oxfordshire, OX11 0DE,  
17 UK

18 <sup>8</sup> Mechanical Engineering, University College London, London, WC1E 7JE, UK

19  
20 **Abstract**

21 **Imaging techniques for quantifying how the hierarchical structure of deforming joints changes**  
22 **are constrained by destructive sample treatments, sample-size restrictions and lengthy scan**  
23 **times. Here, we report the use of fast, low-dose pink-beam synchrotron X-ray tomography**  
24 **combined with mechanical loading at nanometric precision for the in situ imaging, at**  
25 **resolutions lower than 100 nm, of mechanical strain in intact untreated joints under**  
26 **physiologically realistic conditions. We show that, in young, aged, and osteoarthritic mice,**  
27 **hierarchical changes in tissue structure and mechanical behaviour can be simultaneously**  
28 **visualized, and that tissue structure at the cellular level correlates with whole-joint mechanical**  
29 **performance. We also used the tomographic approach to study the co-localization of tissue**  
30 **strains to specific chondrocyte lacunar organizations within intact loaded joints, and for the**  
31 **exploration of the role of calcified-cartilage stiffness on the biomechanics of healthy and**  
32 **pathological joints.**

33  
34  
35 One-sentence editorial summary (to appear right below the article's title on the journal's website):

36 **Pink-beam synchrotron X-ray tomography combined with mechanical loading at nanometric**  
37 **precision enables the in situ imaging of intact untreated joints, resolving strains at sub-100-**  
38 **nm resolution.**

39 Imaging methods have proven essential to our understanding a range of key biomechanical  
40 systems. This has been particularly true for musculoskeletal challenges, such as  
41 understanding a joint's mechanical function, healthy ageing and the impact of changes in  
42 articular cartilage integrity on locomotion. Safeguarding the avascular, aneural articular  
43 cartilage tissue places burden on neighbouring mineralised tissues. Extensive incidence of  
44 degeneration of the entire joint in osteoarthritis is *prima facie* evidence of the likely scale of  
45 this threat. However, current imaging techniques are unable to resolve this detail *in situ*.  
46 Further, joint mechanics are also believed to be dominated by the extracellular matrix of the  
47 hyaline cartilage and by mineralized subchondral regions, where cancellous bone capped by a  
48 cortical plate is found beneath calcified cartilage, which merges with hyaline cartilage. These  
49 tissues are known to retain distinct physiology, structure and mechanics, but how they  
50 interact at the nano-scale to secure healthy joint mechanics under physiologically  
51 representative loading remains undefined. A method for resolving the ultra-structure of the  
52 joint, and in particular, the management of tissue strain as joint compressive stresses are  
53 transmitted from the low stiffness articular cartilage through to the high stiffness cortical  
54 plate is required.

55 Current imaging methods of this key biomechanical system have advanced tremendously, but  
56 each is restricted to either scale or application. Nano-scale imaging in other contexts is now  
57 possible via many approaches<sup>1-4</sup>. For example small-angle and wide-angle X-ray scattering  
58 can yield bone collagen fibril/ mineral phase information as well as 3-dimensional (3D) strain  
59 maps; however, these nano-scale approaches can only measure thin tissue fragments<sup>5-8</sup>, or  
60 average the strain through thickness. Most require a very high X-ray dose, causing damage  
61 and/or limiting the technique to hard tissue. Further, many techniques are only applicable on  
62 thin histological samples due to field of view limitations. This failure to retain organ-level  
63 integrity due to restrictions imposed by scan conditions also arises in ptychography and  
64 focused ion beam scanning and transmission electron microscopy (FIB-SEM/TEM)<sup>9-12</sup>.  
65 Confocal microscopic alternatives for nano-scale imaging require staining to achieve  
66 anisotropic spatial resolution but can be applied only to a very restricted tissue depth<sup>13,14</sup>.  
67 Optical/confocal microscopy with 2D/3D digital image correlation (DIC) is also hampered by  
68 tissue opacity, distorting and limiting the resolution and depth<sup>15-19</sup>. Indentation-atomic force  
69 microscopy delivers nanomechanics, yet is restricted to surface imaging by inefficient 'deep'  
70 probing and tissue processing<sup>20-22</sup>. A method compatible with volumetric, ultra-high  
71 resolution imaging and quantification of mechanical strain during the repeated *in situ*  
72 biomechanical characterisation of hierarchical structure during loading of an intact sample,  
73 such as a whole joint, is therefore highly desirable.

74 Magnetic resonance does allow the probing of whole joints at macroscopic scales, but  
75 imposes limits both upon spatial and temporal resolution. On the other hand, X-ray computed  
76 tomography (CT) yields greater spatial resolution, is nominally non-destructive, attuned to  
77 repeat imaging and offers excellent field of view trade-offs which, together with digital  
78 volume correlation (DVC), can realise full-field continuum- and tissue-level strain  
79 measurement<sup>23-26</sup>. The greater flux and high-end instrumentation in synchrotron computed  
80 tomography (sCT) enables even higher spatial and temporal resolution, making it ideal for  
81 rapid collection of multiple 3D volumes during *in situ* loading. However, sCT may cause  
82 substantial tissue damage and thus beam configuration and scan parameters that maintain  
83 both tissue integrity and tomographic reconstruction quality are required to enable DVC  
84 accuracy. The resolving of *in situ* nano-scale strain in intact mineralized tissues has however  
85 been deemed unattainable<sup>27</sup>. Improved methodologies are required to: i) enhance resolution  
86 without compromising field of view; ii) lessen total radiation exposure to preserve tissue  
87 mechanics<sup>28</sup>; iii) curb sample motion during scanning, and; iv) control *in situ* load application

88 to high levels of precision, in this case, to un-sectioned bones and intact joints. Additionally,  
89 significant advances are also required in DVC algorithms, allowing variable density point  
90 clouds that match the complex shape and internal microstructure of the bones comprising the  
91 joint's structure that matches the imaging technique's resolution.

92 Herein, our sCT method attains greater resolution and imaging speed, allowing for DVC-  
93 based strain fields calculated from displacements with better than 100 nm accuracy within  
94 intact, untreated mechanically loaded mouse bones and knee joints in physiological  
95 orientation. To understand the biomechanical functionality of the joint in health and in  
96 osteoarthritis, we have applied our method to STR/Ort and CBA mouse joints. The STR/Ort  
97 mouse is a well-established, spontaneous model of osteoarthritis, with disease resembling that  
98 in humans. Mice develop articular cartilage lesions predominantly on the tibia plateau, with  
99 other expected degenerative changes coinciding with the attainment of sexual maturity<sup>29</sup>.  
100 CBA mice are the most appropriate control for the STR/Ort mouse as they are the nearest  
101 available parental strain, and extensive analysis reveals they show no overt signs of  
102 osteoarthritis with ageing<sup>29</sup>. We demonstrate how our methods pinpoint many hitherto  
103 unaddressed questions in joint mechanobiology, including the extent to which osteoarthritis-  
104 prone joints exhibit: (i) greater chondrocyte hypertrophy, (ii) abnormally high strains in the  
105 calcified cartilage, (iii) localised calcified cartilage cracking and (iv) development of tissue  
106 strains consistent with a stiffer articular construct. These quantitative imaging methods bridge  
107 gaps between whole joint mechanics and nanoscale strain development in sub-articular  
108 tissues, enabling the elusive structural cartilage-bone hierarchical features underpinning joint  
109 health and disease to be defined.

## 110 **Results**

111 *Fast sCT imaging of nano-resolved load-induced strains in intact mouse joints:* was  
112 enabled via satisfying the challenging trade-off between spatial resolution, field of view  
113 (FOV), signal to noise ratio (SNR), DVC accuracy, radiation dose, and sample motion. To  
114 achieve nano-resolution in intact joints, we employed high-flux/short-exposure continuous  
115 imaging to facilitate high efficacy collection of less damaging high-energy photons, reducing  
116 tissue exposure to ionizing radiation (Suppl. Methods). The high efficacy imaging was  
117 achieved using high and low bandpass filtering, tailored to select harmonics primary centred  
118 at 20 keV, producing a high-flux 'pink' beam<sup>30</sup> coupled to a high dynamic range pco.edge 5.5  
119 sCMOS camera (Fig. 1A and Methods), allowing collection of 2401 projections with 30%  
120 transmission in 4.4 minutes (FOV 4.1x3.45 mm, effective pixel size 1.6  $\mu\text{m}$ , 2401  
121 projections, SNR  $\sim$ 1.4; see Setup 1 in Suppl. Table ST1).

122 Applying these conditions to entire knee joints enabled cell lacunae in the calcified cartilage  
123 (hypertrophic chondrocytes) and subchondral bone (osteocytes) to be readily resolved with  
124 unprecedented resolution for the radiation dose ( $\sim$ 100 kGy; Fig. 1B-E) and speed (Suppl.  
125 Table ST1-Setup 1 and Suppl. Fig. S3c,f). This compares to the equivalent monochromatic  
126 beam setup dose of  $\sim$ 157 kGy and time of almost 40 minutes (Suppl. Table ST1-Setup 4 and  
127 Fig. S3h).

128 The natural tissue 'texture' created by hypertrophic chondrocytes in calcified cartilage and  
129 osteocytic lacunae in subchondral bone is ideal for the reliable measurement of nano-scale  
130 load-induced displacements within the intact joint using DVC. For DVC, the 3D texture is  
131 correlated between a sequence of snapshots capturing the local movement/distortion of the  
132 tissue texture as global load displacements are applied. Therefore, three more advances were  
133 made: firstly, synchronising our unique nano-precision joint motion replicator with  
134 meticulous built-in rotation into the imaging chain (see Methods); secondly, further reducing  
135 the dose (to  $<$ 25 kGy) and scan time (1.1 min, Suppl. Table ST1- Setup 2, and Fig. S3F), and

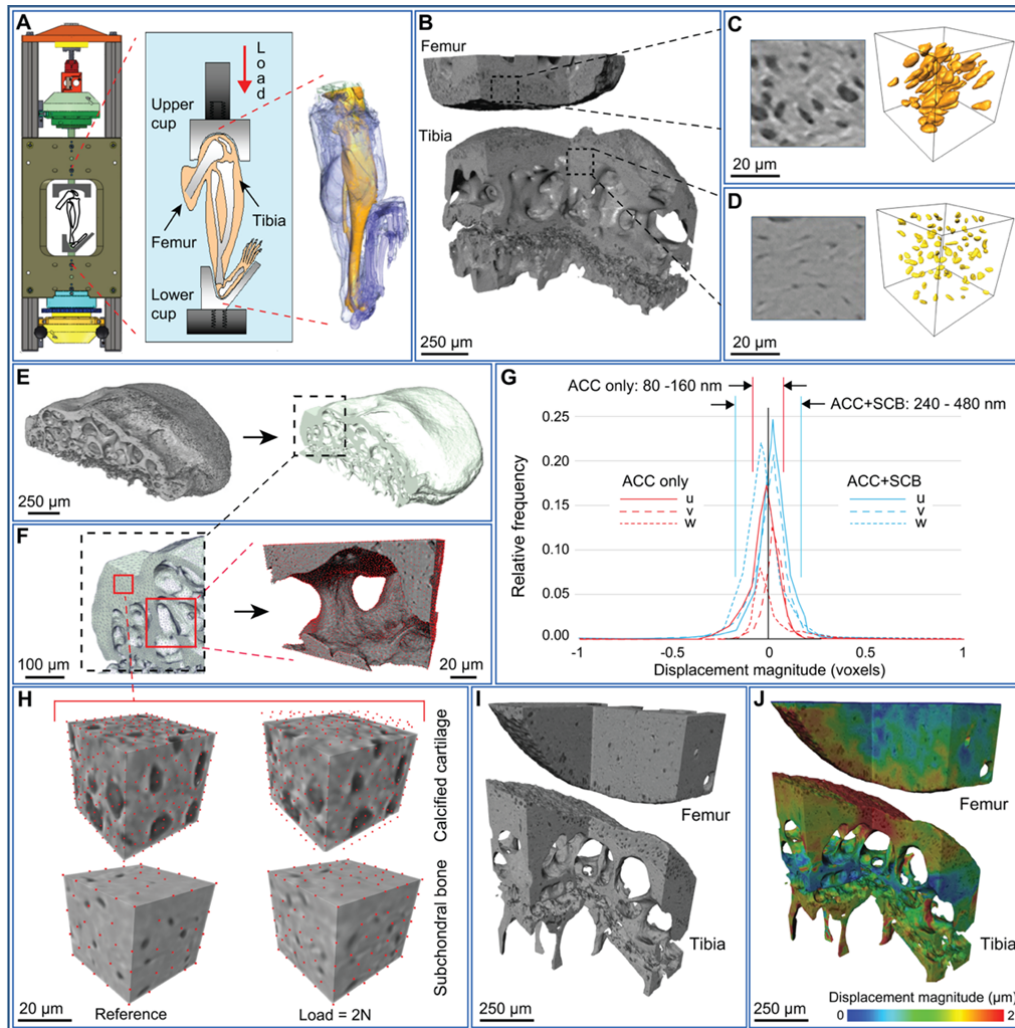
136 thirdly, application of an in-house high accuracy DVC code (Diamond-DVC, open-access,  
137 ccppforge.cse.rl.ac.uk).

138 ***The nano-precision joint motion replicator design:*** was developed by adapting a bespoke  
139 nano-precision tension-compression-torsion rig<sup>31,32</sup> (Fig. 1A) that has air-bearing rotation  
140 within the load train, enabling continuous sample rotation at high speed (>10 rpm),  
141 synchronously with better than 0.001° differential error [see Methods]. Key to avoiding  
142 unwanted off-axis forces and misalignment artefacts during sCT was laser alignment of the  
143 rams rotating on air-bearings to ensure concentricity to better than 50 nm, or <10% of voxel  
144 size. Load measurement accuracy of greater than 0.1 N with 50 nm displacement control was  
145 enabled by pre-scanning of joints and 3D printing the grips/cups to ensure alignment was  
146 conserved during rotation.

147 ***The unique digital volume correlation code:*** allows flexible point cloud specification of sub-  
148 volume locations, concentrating correlation into the regions where displacement values are  
149 sought, preventing subvolumes from locating within voids and overlapping surfaces (Fig.  
150 1)<sup>33</sup>. Discrete DVC sub-volume centres were obtained by extracting nodes using unstructured  
151 3D meshing of the joint generated from tomographic data (Figs. 1F, G). Combined with  
152 customized image processing, DVC point density was readily modifiable in distinct  
153 anatomical joint compartments to allow variable measurement accuracy levels of load-  
154 induced strain to be attained (Fig. 1H).

155 This combination of advances (Fig. 1A,H,K and Fig. 2) allows the generation of 3D full-field  
156 displacements in the subchondral bone and calcified cartilage of a whole joint with 240-480  
157 nm precision (0.3 voxel, Fig. 1H). Accuracy was increased further to yield 80-160 nm  
158 precision (0.08 voxel) when only the calcified cartilage compartment (which has strong  
159 image texture at the micron scale) of the joint was considered (Fig. 1H). This non-invasive  
160 measurement of displacement/strain within whole joints under load demonstrates a facility  
161 for direct measurement of tissue mechanical response across the articular calcified  
162 cartilage/subchondral bone interface for the first time (Fig. 1K), enabling integration with  
163 existing anatomical and organ scale data as well as validation of multiscale finite element  
164 models. When applying loads to whole joints, the deconvolution of the complex 3D  
165 interactions between tissue material properties and structure is, however, difficult. They  
166 nonetheless demonstrate that the distribution and concentration of displacements (and hence  
167 strain) can now be measured across the tibial plateau, even within relatively small areas  
168 (<500 µm or <1/8 of the area), as the femur transfers the applied load. Strain can also be  
169 further localised in the subchondral trabecular struts of the tibia.

170



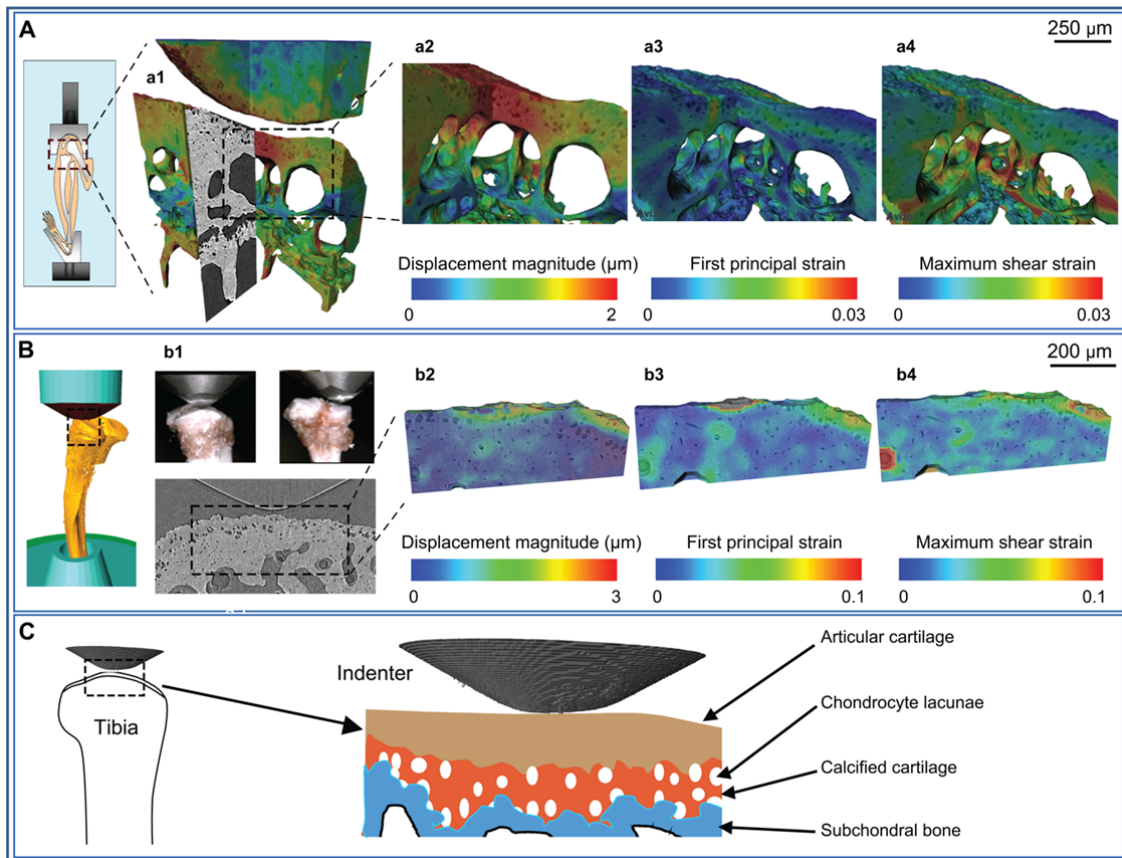
172

173 **Fig. 1 Ultra-high resolution synchrotron computed tomography (sCT) and digital**  
 174 **volume correlation (DVC) of intact joints: (A)** Schematic of *in situ* sCT imaging setup (see  
 175 Suppl. Fig. S1). **(B)** 3D cut-away rendering of sCT data from the medial side of a murine  
 176 knee joint (STR/Ort 20 week), with **(C)** expanded view from articular calcified cartilage  
 177 (ACC) region of the femur showing hypertrophic chondrocyte lacunae as dark regions within  
 178 the sCT data (left) and as rendered voids (right) and **(D)** likewise for osteocyte lacunae from  
 179 subchondral bone (SCB) region of the tibia. Development of DVC point clouds: **(E)**  
 180 rendering of the proximal tibia segmented through a region-growing algorithm (left) followed  
 181 by morphological closure of hypertrophic chondrocyte and osteocyte lacunae (right), and **(F)**  
 182 expanded views showing subsequent tetrahedral finite element mesh (left) and nodes used as  
 183 the DVC point cloud (right). **(G)** DVC displacement precision determined from correlation of  
 184 repeat reference images as  $\pm 1$  standard deviation (indicated by vertical lines) of  
 185 displacement components ( $u, v, w$ ) in the coordinate ( $x, y, z$ ) directions: between 80-160 nm for  
 186 the ACC and 240-480 nm for the entire joint including SCB. Results are representative of  
 187  $n=2$  joints. **(H)** Two subvolumes of size 48 voxels (39  $\mu\text{m}$ ) in reference (left) and deformed  
 188 (right) states with red points representing the point cloud for ACC (top) and SCB (bottom)  
 189 regions (higher density in ACC where strains are higher). **(I)** 3D cut-away rendering of the  
 190 medial aspect of a STR/Ort 40 week joint illustrating femur (top) and tibia (bottom)  
 191 morphologies, and **(J)** superimposed displacement magnitude obtained by DVC.

192

193 To demonstrate use of the technique to probe how the tibia accommodates loading with even  
194 greater precision, an alternative methodology for applying a highly controlled load via a  
195 spherical tipped indenter onto the tibial plateau (where osteoarthritic lesions appear most  
196 prominently in this strain) was developed (Fig. 2). The indenter allows application of  
197 identical, controlled loads to the tibial plateau in both mouse strains at a highly reproducible  
198 location, without anatomical or morphological differences that would otherwise complicate  
199 interpretation. This enables localised mechanical behaviour, particularly material fracture  
200 characteristics, to be probed using region of interest scanning, enabling even higher spatial  
201 strain resolution. The joint was disarticulated, and the tibia and its articular cartilage and  
202 medial meniscus preserved. This was then mounted and a 200  $\mu\text{m}$  radius tip diamond  
203 indenter located directly over the medial plateau. Fig. 2A shows the measured  
204 displacements/strains for relevant non-invasive whole joint loading. Fig. 2B demonstrates  
205 that indentation introduces no imaging artefacts and the tibia sample is stable, allowing  
206 volumetric imaging with resolution suitable for morphological and mechanical response  
207 measurements analogous to those for whole joint loading. This technique was then used to  
208 apply highly controlled loads in 1 N increments (Suppl. Methods) up to failure. These  
209 methods provide data critical to unravelling the relationships between morphological  
210 changes and localised mechanical properties across the calcified cartilage and subchondral  
211 bone interface in both joints of mice that exhibit healthy ageing and those prone to  
212 osteoarthritis (Fig. 2C, discussed below).

213 ***Hypertrophic chondrocyte lacunar size in the osteoarthritis-prone joint:*** Image processing  
214 and surface rendering techniques can be applied to 3D images attained using our  
215 methodology (Fig. 1 & 2) to effectively measure changes, as well as differences, in articular  
216 morphology. For example, we can measure larger hypertrophic chondrocyte lacunar volumes  
217 in the calcified cartilage of a 20-week old STR/Ort (osteoarthritic) murine joint (Fig. 3B & F)  
218 than in an age-matched control CBA (healthy) joint (Fig. 3A & E). The scope to measure  
219 these larger hypertrophic chondrocyte lacunae was also apparent in an ageing 40 week-old  
220 osteoarthritic STR/Ort mouse joint (Fig. 3C, D, G, H, I,  $P < 0.001$ ) which, at this age, was  
221 coupled to a significantly greater thickness in the joint's calcified cartilage tissue layer (Fig.  
222 3J). Direct imaging of intact joints is also useful for revealing greater elongation of these  
223 expanded calcified cartilage hypertrophic chondrocyte lacunae in the STR/Ort than in the  
224 healthy CBA joints (Fig. 3K – Q,  $P < 0.01$ ).



225

226

227

228

229

230

231

232

233

234

235

236

237

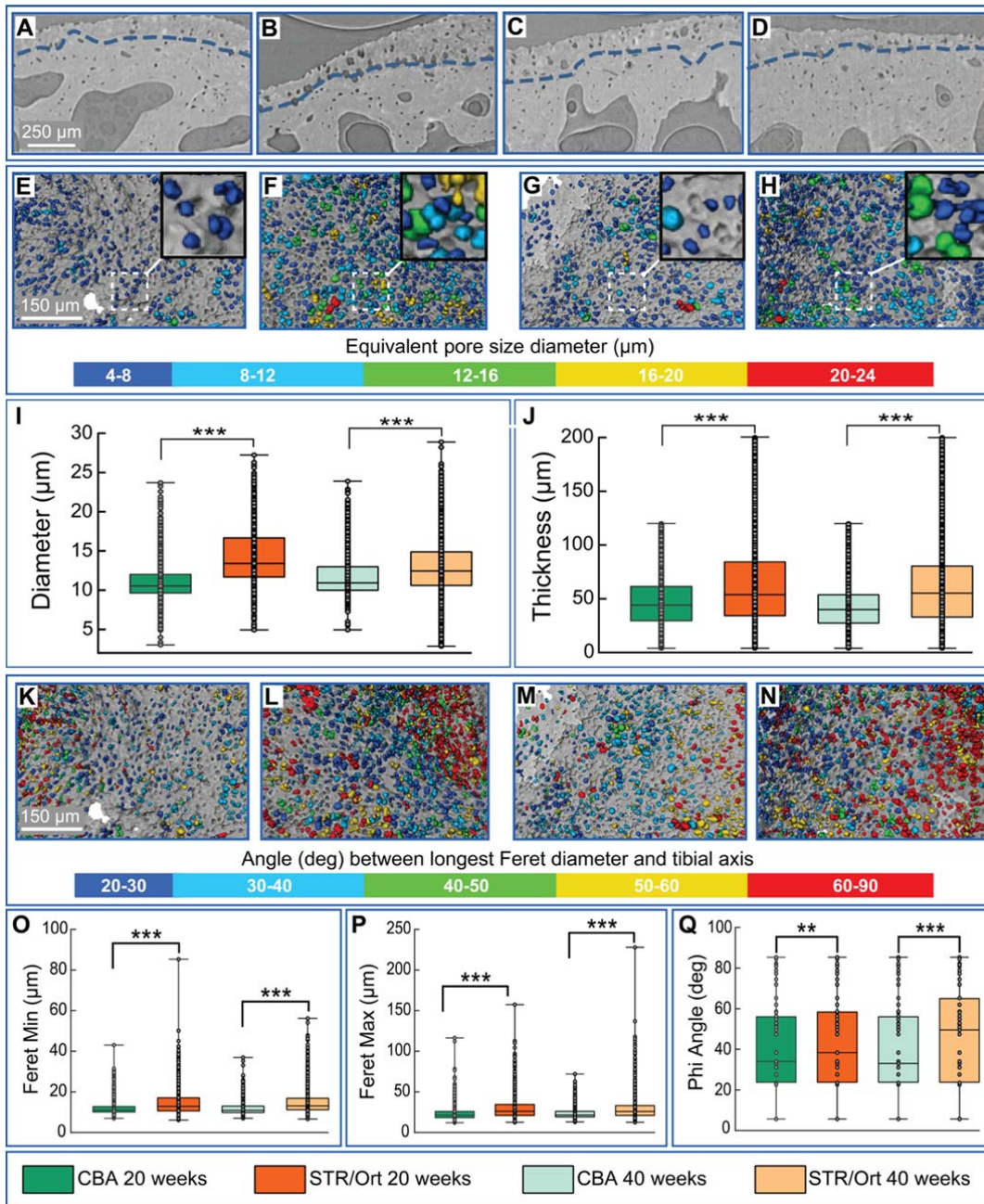
238

239

240

241

**Fig. 2. 3D strain mapping of intact tibia:** (A) Schematic of the full mouse joint loading model (left), (a1) expanded view showing ultra-high resolution imaging (0.8 μm pixel size) of the medial plateau of a 40 week-old STR/Ort mouse ( $n=1$ ) with superimposed displacement field. Further expanded views of (a2) displacement magnitude, (a3) first principal strain and (a4) shear strain fields. The full joint loading configuration is representative of physiologic loading, and closely recapitulates a common *in vivo* experimental protocol. (B) Schematic of indentation loading applied to the disarticulated tibia (left), (b1) lateral (left) and posterior (right) views of the 200 μm tip radius diamond indenter in contact with the medial plateau, and (bottom) representative tomography slice under the indenter showing highly-resolved hypertrophic chondrocyte and osteocyte lacunae of a 40 week-old CBA mouse ( $n=1$ ). Further expanded views of (b2) displacement magnitude, (b3) first principal strain and (b4) shear strain fields within the articular calcified cartilage and subchondral bone regions. Indentation allows highly controlled loading whilst local imaging allows excellent resolution. (C) Schematic highlighting the capability of this method to enable ultra-high resolution imaging during highly controlled indentation, with loading transmitted through the articular cartilage and mineralized subchondral layers.

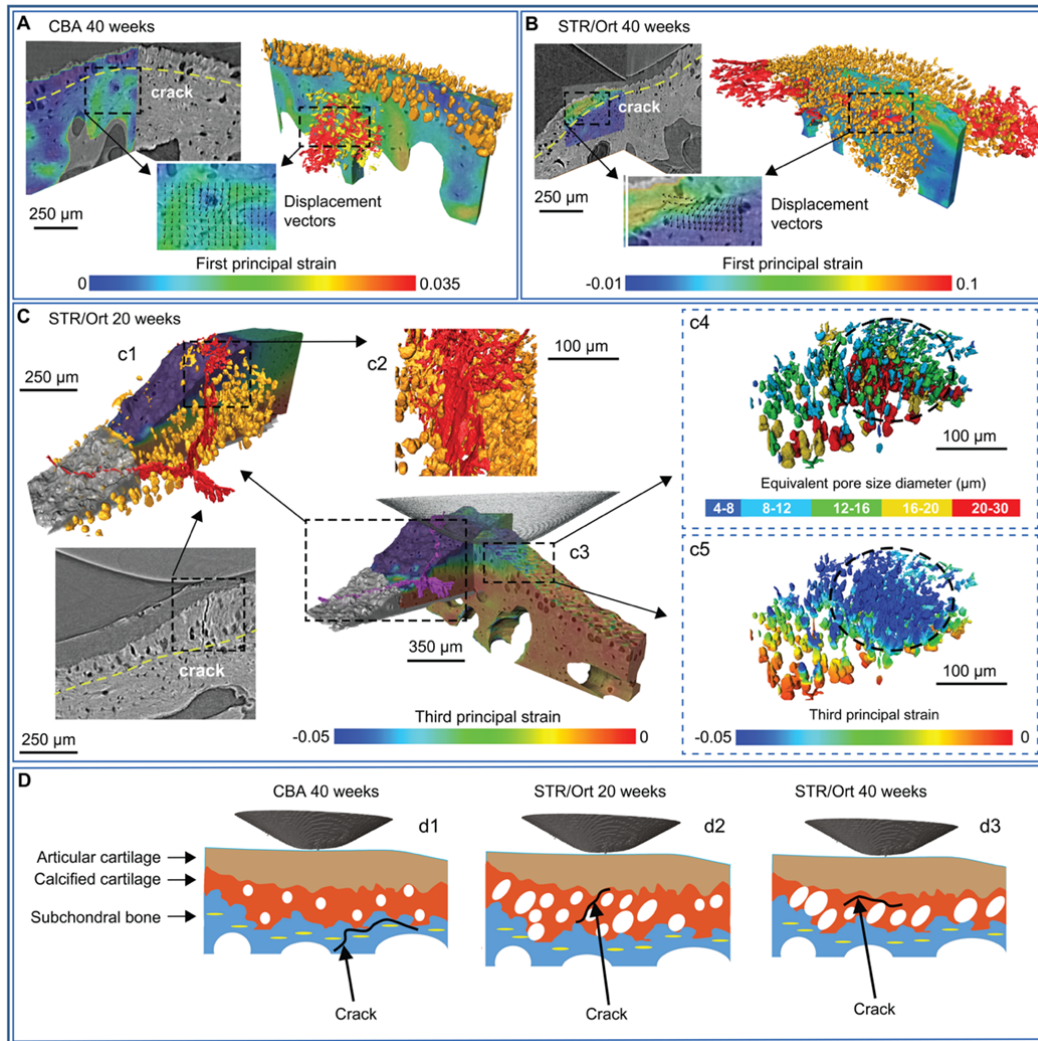


242

243 **Fig. 3. Ultra-high resolution synchrotron CT imaging of calcified cartilage:** Example  
 244 tomography sections from: (A) CBA 20+ week old, (B) STR/Ort 20+ week old, (C) CBA  
 245 40+ week old, and (D) STR/Ort 40+ week old. Calcified cartilage chondrocyte lacunae  
 246 morphology and distribution illustrated for CBA (E-20 wk, G-40 wk) and STR/Ort (F-20 wk,  
 247 H-40 wk), with (I) equivalent volume spherical pore diameter and (J) calcified cartilage layer  
 248 thickness quantified. Depiction of angle between longest lacunae dimension (maximum  
 249 Feret diameter) and tibial axis for CBA (K-20 wk, M-40 wk) and STR/Ort (L-20 wk, N-40  
 250 wk), with (O) smallest dimension, (P) largest dimension, and (Q) orientation quantified.  
 251 Box-whisker plots:  $n=1$  joint in each age/strain with  $n>1000$  individual chondrocytes  
 252 measured in each joint; boxes of 25<sup>th</sup>/75<sup>th</sup> percentiles with median bar and whiskers  
 253 encompass 99% of data points; different from adjacent population with (\*\*\*)  $p<0.001$  and  
 254 (\*\*)  $p<0.01$ .



255 ***Tissue-specific correlation of microfracture surfaces with strain patterns and***  
256 ***morphological features at high spatial resolution:*** With a view to documenting fracture  
257 surfaces, strain patterns and morphological features, we utilized indentation loading to create  
258 localized tissue deformation under the medial condyle of tibiae isolated from a healthy,  
259 ageing control (40 week-old CBA) and from early and late-stage osteoarthritic joints (20 and  
260 40 week-old STR/Ort; Figure 4). Results show an unprecedented level of detail for  
261 localization of deformation and damage in specific subchondral tissues of intact bones. We  
262 observed load-induced fracture only within the deep subchondral bone regions of a healthy  
263 control tibial condyle, with the calcified cartilage layer remaining structurally intact. DVC  
264 strain patterns exhibit high apparent tensile strains associated with the tissue fractures, which  
265 can be difficult to otherwise observe. The relationship between fracture surface and nearby  
266 osteocyte lacunae is also demonstrated through morphological analysis of the imaging data.  
267 In marked contrast, load application in an osteoarthritic 40-week old STR/Ort mouse tibial  
268 condyle instead produced fracture surfaces restricted to the calcified cartilage layer, with an  
269 orientation parallel to and near the overlying condylar layer. A sample of intermediate age  
270 from the osteoarthritic mouse line (20-week old STR/Ort) exhibited intermediate behaviour,  
271 with a complex fracture surface spanning the depth of the calcified cartilage, passing through  
272 a region of clustered large pores and with high apparent compressive strains. These data,  
273 albeit from single representative tibial samples, show that this technique can be used to  
274 explore the evolution of damage within sub-articular tissues and whether osteoarthritis  
275 susceptibility is linked to greater vulnerability to calcified cartilage cracking. Specific  
276 hypotheses concerning load-induced strain can be explored (Figure 4d), with response  
277 mapped directly to observable microstructural features. DVC strain measurement will define  
278 fracture location, orientation and susceptibility and create a basis for evaluation of  
279 microstructural tissue models.



280

281 **Fig. 4. Correlative visualisation of microstructure, strain patterns, and fracture**  
 282 **surfaces:** (A) Fracture surfaces (red) appear deep to the articular surface within subchondral  
 283 bone (below dashed yellow line) in an aged CBA control sample, but (B) shallower, within  
 284 calcified cartilage (above dashed yellow line) in an aged STR/Ort arthritic sample. DVC  
 285 analysis aids fracture identification (red) with localized patterns of high apparent tensile  
 286 strain, and highly resolved spatial association with osteocyte (yellow) and chondrocyte  
 287 lacunae (orange) is demonstrable through morphological analysis. (C) A younger 20 week  
 288 STR/Ort sample exhibits clear fractures through the articular calcified cartilage in  
 289 tomography sections (c1, bottom panel), as part of a complex fracture surface spanning  
 290 between subchondral bone and articular cartilage (c1, c2). Portions of the fracture surface  
 291 (c3) pass through clusters of hypertrophic chondrocyte lacunae in calcified cartilage (c4)  
 292 and exhibit high apparent compressive strains (c5). Results represent analysis of  $n=1/\text{strain}/\text{age}$ .  
 293 (D) These multi-faceted measurements support development of detailed tissue function  
 294 hypotheses: (d1) healthy joint: loads transferred through a stable layer of calcified cartilage  
 295 with small homogeneously distributed chondrocyte lacunae, overload fractures within  
 296 repairable subchondral bone (CBA 40 weeks); (d2) early-stage OA: defective transfer of joint  
 297 loads through larger clustered hypertrophic chondrocyte lacunae, complex trans-calcified  
 298 cartilage fractures (STR/Ort 20 weeks); and (d3) late-stage OA: calcified cartilage thinning

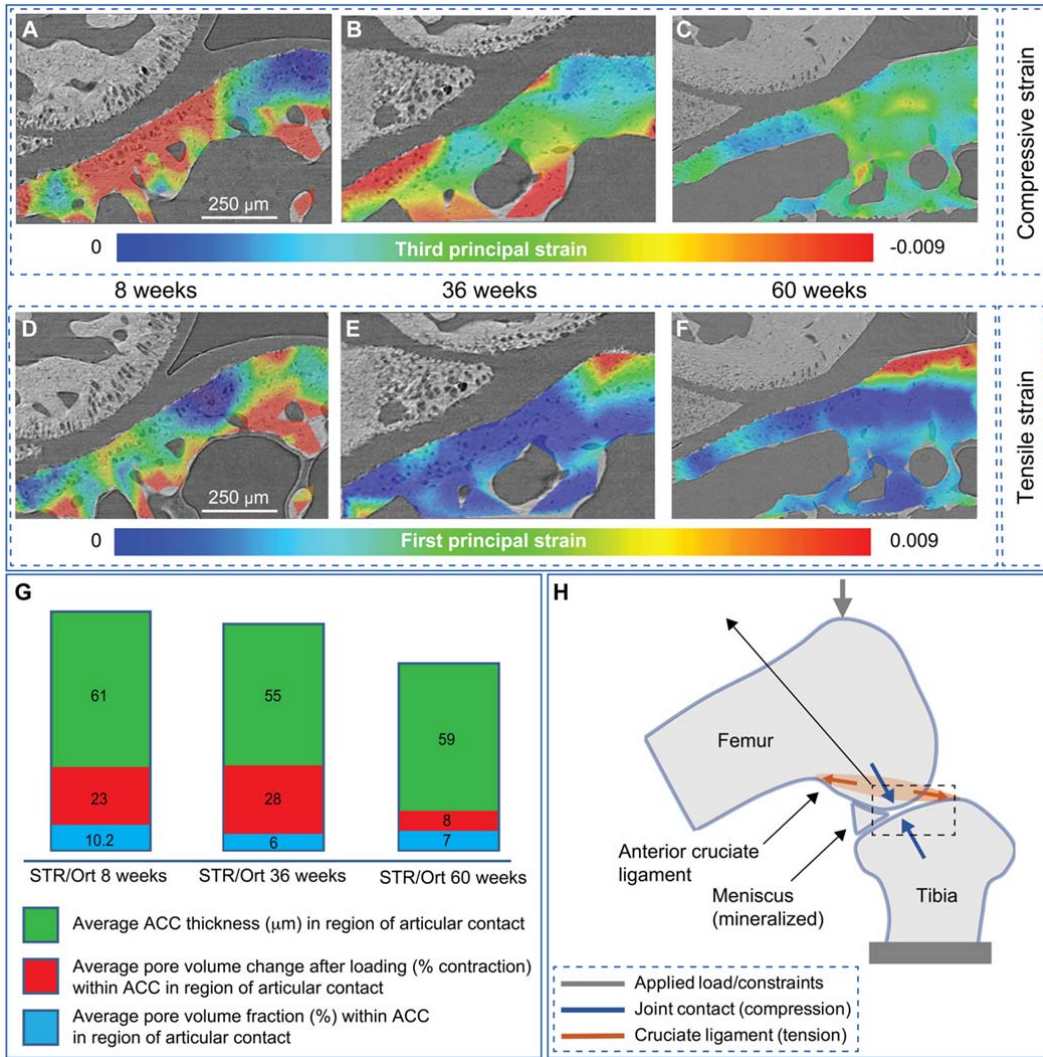
299 and stiffening, with fractures localized to the calcified cartilage/subchondral bone interface  
300 (STR/Ort 40 weeks).

301 ***Quantification of tissue-level strains during physiologically representative whole joint***  
302 ***loading in the STR/Ort mouse model of osteoarthritis progression:***

303 A loading regime was developed to recapitulate steady-state levels achieved during typical  
304 use of the flexed-knee model whilst supporting digital volume correlation. Reference images  
305 were collected by compressing samples at 5 microns/s to a preload of  $1.0 \pm 0.1$  N, waiting 10  
306 minutes for load relaxation, then sCT scanning with sample motion stabilized. Two load steps  
307 increasing peak load by 0.2 N each were then added, with subsequent relaxation and scanning.  
308 Peak loads were then increased into the 2.0 to 2.5 N range for final relaxation and scanning  
309 sequences. Relaxed load levels were approximately half of the peak load levels in all cases  
310 and were stable within the  $\pm 0.1$  N measurement precision of the loading system. Strain maps  
311 (Fig. 5) reflect correlation between the preload and highest applied load scan volumes.

312 The whole-joint methodology was used in a longitudinal sequence within the STR/Ort line  
313 (8, 36 and 60 weeks of age), with a single joint from a mouse at each age/strain evaluated.  
314 Tissue compression in the medial tibial plateau (the osteoarthritis-prone condyle in the  
315 STR/Ort mouse), as documented through minimum (third) principal strain in Fig. 5A, is high  
316 in magnitude prior to osteoarthritis onset (8 weeks) throughout the contact region directly  
317 adjacent to the femoral condyle, mostly through the region of articular calcified cartilage with  
318 some extension into the subchondral bone. At this age, direct femoral contact dominates the  
319 joint compressive loading. By 36 weeks (osteoarthritis) higher magnitude compressive strains  
320 are seen predominantly in the articular calcified cartilage and there is also evidence of  
321 compliance within the deeper bone trabeculae supporting the tibial subchondral mineralized  
322 plate (Fig. 5B). By 60 weeks (advanced osteoarthritis) a very different pattern is observed,  
323 with relatively low levels of tissue compression throughout the direct tibial contact region  
324 and deeper supporting tissues (Fig. 5C). These data indicate a utility for this technology in  
325 revealing general trends in joint tissue mechanics. They pinpoint a need to further study  
326 whether the articular construct shifts from a broadly compliant toward a stiffer structure  
327 before, during or after onset of osteoarthritis and whether this is also partly recapitulated in  
328 healthy, ageing joints.

329 Our methodology also quantifies tissue tension as evidenced by maximum (first) principal  
330 strain. Prior to osteoarthritis onset (8 weeks), highly heterogeneous tissue tension is observed  
331 throughout the medial tibial plateau (Fig. 5D) and these tissue tensions become more uniform  
332 and decrease in magnitude with osteoarthritis development at 36 weeks (Fig. 5E), and more  
333 so at 60 weeks of age (Fig. 5F). The fact that these changes can be measured indicates that  
334 the methods allow an examination of the role of microstructure in strain development. Our  
335 data also evidence the scope to map these load-induced tissue strains directly to changes in  
336 tissue structure. In the samples studied here tissue strain changes are measured in parallel  
337 with articular calcified cartilage morphological characteristics measured at high spatial  
338 resolution (Fig. 5G). Our observations of nano-scale resolved strains in intact loaded joints  
339 also allow emerging high tensions at the tibial insertion of the anterior cruciate ligament prior  
340 to osteoarthritis onset to be examined (8 weeks; Fig. 1D) (arrow). With osteoarthritis  
341 development at 36 and 60 weeks, this region of tensile strain has expanded (Fig. 5E & F), and  
342 dominates the strain pattern.



343

344 **Fig. 5. Nano-resolved strain under physiologically representative loading prior to and**  
 345 **after the onset of osteoarthritis:** (A,D) STR/Ort 8+ week, (2.4/1.2±0.1N), prior to onset of  
 346 osteoarthritis (B,E) STR/Ort 36+ week, (2.4/1.4±0.1N), post osteoarthritis onset, and (C,F)  
 347 STR/Ort 60+ week, (2.2/1.2±0.1N), advanced osteoarthritis. Applied loads are shown as  
 348 (peak/relaxed ±1 standard deviation), with preloads for strain measurement of 1.0/0.5±0.1N.  
 349 A single joint from a mouse at each age/strain was evaluated. (A-C) Tissue compression  
 350 (third principal strain) evolves during different stages of osteoarthritis progression. (A)  
 351 Distributed strain under the femoral condyle that permeates throughout the articular calcified  
 352 cartilage and into the subchondral bone in the knee joint of an 8 week-old mouse. (B) At 36  
 353 weeks, compression localizes more, shifting to a location adjacent to the now hypertrophied  
 354 mineralized meniscus. (C) By 60 weeks the pattern is very different, with relatively low  
 355 levels of tissue compression throughout the direct tibial contact region and deeper supporting  
 356 tissues. (D-F) Tissue tension (first principal strain) also evolves with age. Magnitudes are  
 357 initially high in the articular contact regions, but low at 36 weeks and beyond. In contrast the  
 358 anterior cruciate ligament location on the tibial plateau exhibits low magnitude tensile strain  
 359 initially followed by a higher magnitude and more expansive region as age increases. (G)  
 360 Articular calcified cartilage (ACC) thickness, the average chondrocyte lacunae pore volume,  
 361 and the change in chondrocyte lacunae pore volume under load. (H) Schematic of the  
 362 standard loading model used.<sup>34</sup>

363 **Discussion**

364 Our methodology bridges the gap between whole joint mechanics and nanoscale strain  
365 measurement in sub-articular tissues, which will allow the elusive structural cartilage-bone  
366 features underpinning joint health to be defined. These techniques can clearly be used to  
367 reveal hierarchical changes in tissue structure and mechanical behaviour. They show that it is  
368 possible to examine whether strategies for adapting to physiologically representative  
369 mechanical joint loading diverge in diseased joints and that early changes in calcified  
370 cartilage structure are worthy of study, as they may prefigure disease onset. These data  
371 provide the enabling technology for the role of sub-hyaline mineralized tissue microstructure  
372 in strain development to be explored. They also signpost a specific and vital mechanical role  
373 for stiffening in this calcified cartilage layer in disease progression (Fig. 5).

374 A major challenge in osteoarthritis research is understanding the intimate interactions  
375 between the adjoining joint tissues. This challenge is perhaps most obvious, specifically in  
376 the biological and physical crosstalk between the articular cartilage and subchondral bone,  
377 where the calcified cartilage layer is found sandwiched<sup>35</sup>. Indeed studies have shown that this  
378 crosstalk can be facilitated by vessels reaching from the subchondral bone into the calcified  
379 cartilage; patches of uncalcified hyaline cartilage being in contact with the subchondral bone,  
380 and microcracks and fissures extending through the osteochondral unit<sup>36</sup>. Previous studies  
381 have either scanned and examined deformation and ensuing crack formation in a single bone  
382 at the micron scale<sup>37</sup> or have probed surface and near-surface mechanical properties at the  
383 nano-scale in isolated tissue segments<sup>20</sup>; our technique allows the direct measurement of  
384 mechanical strains in intact joints under controlled and physiologically realistic loading  
385 conditions. Several studies have used diffraction or small-angle X-ray scattering to measure  
386 strain, but again this was only achievable in extracted bone fragment samples<sup>38,39</sup>.

387 Our studies have gleaned information across the entire osteochondral unit by combining the  
388 use of two joint loading protocols - an indenter and a non-surgical knee joint loading model –  
389 together with ultra-high resolution imaging of intact mouse knee joints from control and  
390 osteoarthritis-prone strains. The indenter protocol allows application of identical, controlled  
391 loads to the murine tibial plateau at a highly reproducible location, without anatomical or  
392 morphological differences that would otherwise complicate interpretation. The large radius  
393 indenter (with respect to tibial plateau curvature) therefore allows more controlled and  
394 consistent probing of localized mechanical response. It is recognised that the precise tilt  
395 (angle or articulation) of the tibial plateau does show some variation between samples, and  
396 that this may be a factor contributing to tissue strain development. We used a vertical  
397 orientation of the indenter and contact with the middle of the tibial plateau as a means of  
398 creating consistent force input into the samples and to allow the effects of multiple geometric  
399 and material influences to manifest without attempts to adjust for any particular factor. Future  
400 studies using our method described herein will enable the material property and geometry  
401 influences on tissue strain to be examined.

402 Whilst the hierarchical structural and mechanical properties of the adjoining joint tissues are  
403 known to be dissimilar<sup>40</sup>, there is currently little awareness of how tissue strains manifest or  
404 whether mechanical properties across the osteochondral unit vary during healthy and  
405 pathological ageing of the joint. The calcified cartilage is clearly crucially located, linking the  
406 underlying, extensively vascularised subchondral bone through a mineralised interface with  
407 discontinuous, unmatched, collagen type I and II fibres, to the hyaline cartilage where a  
408 continuous traverse of collagen type II fibres abruptly transition from calcified into overlying  
409 non-mineralised cartilaginous tissue. The calcified cartilage is approximately 100 times  
410 stiffer than the overlying hyaline cartilage and 10 times less stiff than the underlying  
411 subchondral bone<sup>41,42</sup>. It is therefore unsurprising that the calcified cartilage layer is thought

412 to be integral to load transmission from the compliant hyaline cartilage, to the underlying stiff  
413 subchondral bone<sup>42</sup>. Indeed alterations in the calcified cartilage thickness, represented by the  
414 balance between the rate of tidemark advancement into the hyaline cartilage and the rate of  
415 calcified cartilage resorption at the osteochondral interface, are associated with increased risk  
416 of joint injury<sup>43</sup>. Our technique was also applied to healthy murine joints, allowing load-  
417 induced strain localisation to be measured in the joint calcified cartilage and underlying  
418 subchondral bone (Fig. 5). Our technology permits examination of new questions: is joint  
419 function safe-guarded by the calcified cartilage? Does joint health rely on structural  
420 robustness at its two interfaces? Whilst these principles would be novel, they are nonetheless  
421 consistent with previous data showing the role of the calcified cartilage in preserving the  
422 structural integrity of the articular cartilage and in regulating subchondral bone mass and  
423 architecture.

424 The stiffness gradient from the subchondral bone to the calcified cartilage may be attributed  
425 to mineralisation status. Reports of lower subchondral bone mineralisation and stiffness have  
426 indeed been reported in osteoarthritis<sup>44-48</sup> and, similarly, alterations in the stiffness gradient  
427 from the calcified cartilage to the subchondral bone are observed at the macro-level in  
428 association with early degenerative changes<sup>42</sup>. Our data suggest that the transfer of high joint  
429 loads to the underlying subchondral bone should be examined further as a potential means by  
430 which healthy joint architecture is preserved; this is consistent with high vascularisation and  
431 scope for rapid and ordered remodelling of subchondral bone. The effectiveness of this  
432 transfer of high joint loads to the subchondral bone is also consistent with our findings  
433 indicating selective, longer term increases in subchondral plate thickness at these loaded joint  
434 locations *in vivo*<sup>49</sup>. Our methods also allow localised inhomogeneity in the strains to be  
435 observed, with some regions exhibiting strains much higher than the nominal, homogenized  
436 values that traditional testing reveals. This is consistent with both measurement and  
437 modelling of mechanical response to load across a broad range of hierarchical scales within  
438 bone and other biological tissues<sup>20,50</sup>. As our measurements are more spatially resolved than  
439 prior work, this broad distribution of strain magnitudes is not unexpected.

440 The presence of cracks in the joint calcified cartilage has been recognised for some time,  
441 however their significance had remained undetermined<sup>51</sup>. It has been postulated that  
442 microcracks in the osteochondral interface may enable the transfer of molecules and  
443 substances to the hyaline cartilage, from which it is normally protected<sup>52,53</sup>. For example,  
444 subchondral-derived inflammatory cytokines and growth factors that have been shown to be  
445 detrimental to chondrocyte health<sup>35</sup>. The thickness and porosity of the cartilage and bone in  
446 both human and equine samples also influences bone-cartilage interface transfer<sup>54</sup>.  
447 Furthermore, microcrack propagation may also contribute to the mechanical failure of the  
448 joint when placed under high loads, as has been shown in Thoroughbred horse joints<sup>55</sup>. The  
449 hypothesis that greater levels of calcified cartilage chondrocyte hypertrophy predispose  
450 greater strain concentration, load-induced microcracking and osteoarthritis, is underpinned by  
451 our studies.

452 The idea that mechanical failure may indeed occur in close proximity to the calcified  
453 cartilage has recently been supported by the seminal description of hyperdense mineralised  
454 protrusions (HDMP) from the subchondral plate in joints from Thoroughbred racehorse and  
455 more recently in human osteoarthritic hips<sup>56-59</sup>. These HDMPs comprise a hypermineralised  
456 infill material which may be an extension of a crack self-healing mechanism observed in  
457 bone<sup>60</sup>. Our technique described herein will enable the tracking of strain fields during HDMP  
458 development to potentially validate their proposed method of formation.

459 Mechanics and genetics are prime determinants of healthy joint ageing. Links to genetic  
460 selection for rapid growth also exist<sup>61</sup> and recent research has prompted speculation that  
461 hyaline cartilage chondrocytes ‘switch’ from an inherently stable to a transient phenotype,  
462 similar to that observed in the growth cartilage<sup>62-64</sup>. This transience, vital for longitudinal  
463 bone growth, contrasts however with the stable hyaline chondrocyte phenotype required to  
464 assure life-long joint integrity. The data we have presented herein examining hypertrophic  
465 chondrocyte lacunae size conform with other studies highlighting a contribution of phenotype  
466 switching to the demise of the joint and is consistent with our previous work which  
467 investigated the expression of molecular markers of chondrocyte hypertrophy in these  
468 STR/Ort mice<sup>63</sup>. This revealed an expected pattern of type X collagen expression in the  
469 unaffected (lateral) condyles of STR/Ort mouse joints, with immunolabeling restricted to  
470 hypertrophic chondrocytes. Consistent with our data here, an increased type X collagen  
471 immunolabeling was observed throughout the medial (affected) condylar articular cartilage  
472 matrix in 8–10-week-old STR/Ort mice, before histologically detectable osteoarthritis. Also,  
473 consistent with our findings here, an additional marker of chondrocyte hypertrophy, MMP-  
474 13, was detected to be increased in the calcified cartilage chondrocytes of STR/Ort mice<sup>63</sup>.  
475 Together these data warrant further investigation into the role of chondrocyte hypertrophy in  
476 the calcified cartilage in generating the abnormal strain localisation observed in osteoarthritic  
477 joints. Interlinks between these discordant phenotypes are however not fully deciphered and  
478 whilst the hypothesis that limited ‘switching’ contributes to preserving joint health is  
479 controversial, our newly described methods will undoubtedly provide clear insights into the  
480 mechanical role of chondrocyte hypertrophy in osteoarthritis.

481 The utility of our whole loaded joint imaging and DVC approach is perhaps best exemplified  
482 by the generation of unique, first of their kind, 3D full-field displacements and strains in the  
483 intact mineralised joint tissues (Fig. 5), indicating potential for future studies examining the  
484 interplay between genetics and mechanics in joint health and osteoarthritis. Our findings  
485 provide a means for generating new hypotheses in significant orthopaedic healthcare  
486 challenges such as osteoarthritis, as we have done here. However, one limitation of our study  
487 is the difficulty in obtaining data from a large number of replicate animal joints for statistical  
488 validation of these hypotheses, as synchrotron access for performing these ultra-high  
489 resolution *in situ* imaging is limited. The technique we have developed will nonetheless have  
490 a wide range of applications, for example, in orthopaedics measuring strain in both healthy  
491 joints and the impact of joint replacements on strain distributions. For osteoarthritis, these  
492 new insights provide a viable model system for the efficacy of new treatments to be explored  
493 in longitudinal studies, potentially shortening the drug development pipeline. They also  
494 expand studies across the length scales, from nanoscale resolution of the osteochondral unit  
495 to the whole joint. Further, the technique is applicable to many non-biological systems where  
496 strain measurements are required at the nano-scale with minimal radiation damage *in situ* or  
497 *operando*.

## 498 **Methods**

### 499 **Animals**

500 Male STR/Ort (bred in-house at the Royal Veterinary College) were examined before  
501 osteoarthritis onset (8 weeks), at early osteoarthritis onset (20 weeks) and late osteoarthritis  
502 (40 weeks) in comparison to male age-matched CBA mice (Harlan UK Ltd. UK). CBA mice  
503 are the most appropriate control for the STR/Ort mouse as they are the nearest available  
504 parental strain, and extensive analysis reveals they show no overt signs of osteoarthritis with  
505 ageing<sup>29</sup>. Mice were kept in polypropylene cages, with light/dark 12-h cycles, at  $21 \pm 2^\circ\text{C}$ ,  
506 and fed ad libitum with maintenance diet (Special Diet Services, Witham, UK). All



507 procedures complied with Animals (Scientific Procedures) Act 1986, were approved by the  
508 local ethics committee of the Royal Veterinary College, and comply with the ARRIVE  
509 guidelines. STR/Ort mice were maintained by brother/sister pairing<sup>29</sup>. Whole hind limbs were  
510 dissected and stored frozen at -20°C. Knee joints were either scanned as intact limbs, or were  
511 dislocated on the day of scanning, all soft tissues removed from the distal tibial element  
512 before it was severed close to the midshaft with a bone saw. All samples, both intact joints  
513 and disarticulated indentation samples, were maintained hydrated in phosphate buffered  
514 saline during all scanning<sup>29</sup>.

### 515 **In situ testing using bespoke nano-precision rig**

516 Our bespoke in situ mechanical rig<sup>65</sup> (P2R; Fig.1 and Suppl. Fig. S1) was designed with a  
517 granite base frame, two rotation shafts coupled with air bearings and servomotor assemblies,  
518 a load measurement system and its associated drive specifically for in situ X-ray tomography  
519 studies<sup>31,32,66</sup>. Full details are in Supplementary Methods, with only key attributes detailed  
520 here. The air bearings ensure frictionless axial movement of shafts engineered for permanent  
521 alignment accuracy of better than 50 nm, which is required during scanning to avoid  
522 misalignment artefacts and unwanted off-axis forces. Rotation shaft ends are fixed to pre-  
523 aligned micrometre-resolution X-Y translation stages (T12XY, Thorlabs) and aligned  
524 specimen (intact knee joint) are biofilm-sealed to limit dehydration and loaded using custom-  
525 built, 3D printed plastic cups designed to allow axial compression with sub-micron precision  
526 displacement steps to be applied across a flexed knee joint<sup>67</sup>.

527 For dislocated tibias, the mid-shaft was embedded in 1.5 mm of acrylic resin in the pre-  
528 aligned lower cup<sup>68</sup> and specimens indented from above on the centre of the tibial medial  
529 plateau using a 120° diamond Vickers indenter with a 200 µm radius tip (Gilmore Diamond  
530 Tools, Inc.) with 10 micron displacement steps applied and measured loads reaching a  
531 maximum of 4N (note in the whole joint experiments 20 micron displacements were used). A  
532 fifteen minute-window was allowed after loading to avoid motion artefacts during scanning  
533 caused by stress relaxation. All the tests were carried out in wet conditions using a phosphate  
534 buffered solution (PBS)-filled environmental chamber placed in the P2R rig.

### 535 **Ultra-high resolution, fast pink beam imaging**

536 Ultra-high resolution imaging during indentation of the tibia and compression of intact joints  
537 under realistic loading conditions was performed using the Diamond-Manchester Imaging  
538 Branchline I13-2<sup>69,70</sup> of the third-generation synchrotron Diamond Light Source.  
539 Traditionally, monochromatic X-rays have been used for phase contrast enhanced images of  
540 bone<sup>27,71,72</sup>; instead we used a ‘pink beam’ to enable similar data quality with shorter  
541 acquisition times. Sample deformation represents a major obstacle to high-resolution  
542 tomography for joints under compression, and rapid imaging with a pink beam was essential  
543 to enabling this. Here the spectral distribution is determined by the design of the synchrotron,  
544 the insertion device (ID) settings and the choice of filters and mirrors. The resulting beam  
545 (once filtered as below) at I13-2 is ~100 times more intense than a monochromatic beam  
546 generated by a monolayer monochromator<sup>30</sup>. We used the Diamond mini-beta undulator (2 m  
547 long U22 undulator, 2.2cm period length) from which radiation from 90 periods interferes  
548 coherently to produce sharp peaks at harmonics of the fundamental frequency (Suppl. Fig.  
549 S3a). Using a 5 mm ID gap (deflection K~1.743), X-rays of 5-30 keV and flux density of  
550 about  $[[6 \times 10]^{13} \text{ ph/s/} [\text{mm}]^2]$  (flux simulations are detailed in Supplementary  
551 Methods) were generated. Radiation was then selectively filtered to attenuate low energy X-  
552 rays, protecting instrumentation and reducing tissue radiation dose. Filters were used (C-1.3  
553 mm, Al-3.2 mm, and Ag-75 µm) to tune the flux to about  $[[4 \times 10]^{11} \text{ ph/s/} [\text{mm}]^2]$ ,  
554 using 6 harmonics between 16 and 25 keV (Suppl. Fig. S3a), approximately 10 times more

555 than the monochromatic flux (setup 4, E=19 keV, see Suppl. Table ST1). Here, our strategy  
556 is to use less photons at lower energies to reduce the mean energy imparted to the tissue by  
557 ionizing radiation. We satisfied these requirements by suppressing most of the harmonics  
558 below 19 keV (Suppl. Fig. S3b). Slits were used to truncate the beam just outside the field of  
559 view; this reduces both sample exposure and the intensity of noise arising from scintillator  
560 defects. We collected in fly-scan mode up to 4001 high-count projections with a transmission  
561 between 20-40% (effective pixel size of 1.6  $\mu\text{m}$  using setup 1 and 0.8  $\mu\text{m}$  using setup 3, see  
562 Suppl. Table ST1) in less than 7.3 minutes, by means of our precise mechanical rig with  
563 built-in rotation coupled to a fast, high dynamic range pco.edge 5.5 camera (16 bit, 100 fps)  
564 mounted on a scintillator-coupled microscope of variable magnification.

### 565 **Radiation dose**

566 Similar to Pacureanu et al. (2012) a method was developed to measure the signal-to-noise  
567 ratio (SNR) from the images and evaluate the radiation dose from the simulated flux<sup>73</sup> (see  
568 Supplementary Methods). Prior to analysis, our simulations were compared with flux  
569 experiments obtained on the Diamond-Manchester Imaging Branchline and a good agreement  
570 was obtained (Suppl. Fig. S4). The dose rate ranges between 0.4-0.5 kGy/s, which is in the  
571 range of dose rates obtained at different synchrotron locations (Suppl. Table ST2). The trade-  
572 off between scanning time, SNR, and total dose is depicted in Suppl. Fig. S3c-f. The total  
573 dose for each tomogram ranges from 100 kGy (setup 1) to 240 kGy (setup 2) for a 4-7 minute  
574 scan time, which is above the acceptable irradiation levels for in situ bone mechanics<sup>27</sup>. For  
575 comparison, our equivalent monochromatic beam setup (Suppl. Table ST1, setup 3) had a  
576 total dose of about 157 kGy/tomogram but the scanning time is 5 times higher and the SNR 3  
577 times lower (Suppl. Table ST1 and Fig. S3h). Reducing the number of projections to 600 in  
578 pink beam (~1.1 minute scan time, Suppl. Table ST1 - Setup 2) reduces total dose to 27  
579 kGy/tomogram (Suppl. Fig. S3e) such that hypertrophic cells are still resolvable but  
580 osteocyte lacunae are progressively lost (Suppl. Fig. S3c, d, e).

### 581 **Data processing prior to Digital Volume Correlation (DVC)**

582 Reconstruction was performed with the tomography reconstruction module of Dawn 1.7<sup>74,75</sup>,  
583 with normalisation (forty flatfield and darkfield images) and ring artefact suppression prior to  
584 filtered back projection. Prior to DVC analysis, the tomograms were cropped, normalised and  
585 3D median filtered (kernel size 2). Input to the 3D texture correlation texture algorithm  
586 consists of two 8-bit image volumes (non-deformed/deformed) and a flexible point cloud file  
587 that specifies the subvolume locations where displacement values are sought. We developed a  
588 method to generate discrete DVC points analogous to the nodes where a displacement-based  
589 FEA (finite element analysis) calculates displacement results (Fig. 1). Images were imported  
590 into Avizo 9.0 software to create binary region of interest masks (femur/ tibia in intact joints  
591 and calcified cartilage/subchondral bone in the indent specimens). Masks were obtained by  
592 image processing using a region-growing algorithm and then a morphological closure process  
593 to fill porosity from subchondral bone and calcified cartilage (Fig. 1E). Images were then  
594 eroded by 8 voxels to avoid surface edge effects during the correlation process and then used  
595 to generate unstructured tetrahedral finite element (FE) meshes (Fig. 1F) by the well-defined  
596 methodology<sup>76</sup>. Finally, mesh nodes were extracted to define the point cloud (Fig. 1G) and  
597 high density points created to capture high strain gradients.

### 598 **Nanoscale displacements extracted from DVC**

599 3D displacement vector fields were calculated using the diamond.dvc open access code<sup>25,33</sup>.  
600 A Gauss–Newton minimization is applied with cubic spline volumetric image interpolation to  
601 an objective function, defined as the normalised squared differences between subvolumes in

602 the non-deformed and deformed image data, allowing displacements to be measured with  
603 subvoxel accuracy. To assess the *a priori* performance of DVC analysis, correlation of repeat  
604 reference images was performed (Fig. 1H) with standard deviation of measured displacement  
605 vector components used to quantify precision and allow adjustment for imaging noise and  
606 heterogeneous texture. There is generally trade-off between measurement uncertainty and  
607 resolution (Suppl. Fig. S3i) and 40-50 voxels subvolume size (32-40  $\mu\text{m}$ ) produced the best  
608 compromise with a 0.3 voxel DVC accuracy, if the point cloud is homogeneously distributed;  
609 0.8-1.6  $\mu\text{m}$  pixel size allowed displacements in subchondral bone and calcified cartilage to be  
610 measured with 240-480nm accuracy. Regardless of dose, accuracy was increased to 0.08  
611 voxel (~80-160 nm precision) if only calcified cartilage was considered (Fig. 1H, Suppl.  
612 Table ST1 and Suppl. Figs. S3c-f).

613 A critical step in all DVC methods is selection of an accurate starting point in the vicinity of  
614 a global minimum and avoidance of secondary local minima<sup>33</sup>. To redress this, raw images in  
615 non-deformed and deformed states were co-registered using a robust iterative optimization  
616 algorithm (Avizo 9.0) to remove the rigid body motion (translation and rotation). Each  
617 deformed image was then registered with the reference image using the diamond.dvc code.  
618 Correlation quality was assessed by reference to magnitude of the objective function returned  
619 by the correlation process. Histograms of normalised correlation revealed very low and  
620 tightly grouped residuals, indicative of a good match. Point cloud location displacements  
621 were interpolated at a set of grid points using Delaunay triangulation and all Green-Lagrange  
622 strain components were computed using a centred finite differences scheme. The code  
623 modules for strain calculations were modified (from <sup>77</sup>) to include the scattered point  
624 interpolation and all the principal strain components.

### 625 **Statistical analysis**

626 Normality and homogeneity of variance of all the data were checked, and two-sided one-way  
627 ANOVA conducted to compare groups.  $p < 0.05$  was considered to be significant and noted  
628 as \*; p-values of  $<0.01$  and  $<0.001$  were noted as \*\* and \*\*\*, respectively. In situ indentation  
629 experiments were performed on two different 20-week STR/Ort mice, at four loading steps.  
630 Similar strain patterns in the calcified cartilage are found for the two specimens (see Suppl.  
631 Fig. S5a). Higher magnitude compressive strains are seen predominantly in the articular  
632 calcified cartilage. The strain histograms of the first and third principal strains are similar and  
633 appear as asymmetrical distributions (Suppl. Fig. S5b). Animations showing the progressive  
634 compression of the hypertrophic chondrocytes in a transverse section are available for  
635 visualisation in Suppl. Video SV2.

### 636 **Data availability**

637 A representative sample of research data from the experiments along with the plot data for  
638 the graphs in this manuscript is provided in supplementary material. The underlying data are  
639 not provided online due to their size but are available on reasonable request from the  
640 corresponding authors.

### 641 **Acknowledgements**

642 We are grateful to Professor Roger Mason (Imperial College London, UK) for providing our  
643 original STR/Ort mice and for advice on their use. We thank Loic Courtois, Steven Van  
644 Boxel, Catherine Disney, Gowsihan Poologasundarampillai, Jin He, David Eastwood,  
645 Kazimir Wanelik, Ulrich Wagner and Jon Thompson for their help during the beamtimes. We  
646 gratefully acknowledge the Engineering and Physical Sciences Research Council (grants  
647 EP/I02249X/1, EP/M009688/1), Arthritis Research UK (grants 18768 and 20581) and MRC  
648 (MR/R025673/1). Facilities and research support were provided by the Diamond-Manchester

649 Branchline (I13-2) at Diamond Light Source (Beamtimes MT13237-1, MT11076-1,  
650 MT5003-1), and the Research Complex at Harwell.

#### 651 **Author contributions**

652 Conception and design of the study: PDL, AAP, KM, KAS and BB. Acquisition of data: KM,  
653 BB, HG, BJ, KAS, AJB. Interpretation of data, revising the manuscript and final approval,  
654 and agreement to be accountable for all aspects of the work: all authors. Drafting the  
655 manuscript: KAS, KM, BB, AAP, PDL.

#### 656 **Competing interests.**

657 All authors declare no competing financial interests.

#### 658 **References**

- 659 1 Denk, W. & Horstmann, H. Serial block-face scanning electron microscopy to  
660 reconstruct three-dimensional tissue nanostructure. *PLoS biology* **2**, e329 (2004).
- 661 2 Georgiadis, M., Mueller, R. & Schneider, P. Techniques to assess bone ultrastructure  
662 organization: orientation and arrangement of mineralized collagen fibrils. *Journal of*  
663 *the Royal Society Interface* **13**, 20160088 (2016).
- 664 3 Pabisch, S., Wagermaier, W., Zander, T., Li, C. & Fratzl, P. in *Imaging the*  
665 *Nanostructure of Bone and Dentin Through Small- and Wide-Angle X-Ray Scattering*  
666 Vol. 532 *Methods in enzymology* 391-413 (Elsevier, 2013).
- 667 4 Zhu, F.-Y. *et al.* 3D nanostructure reconstruction based on the SEM imaging  
668 principle, and applications. *Nanotechnology* **25**, 185705 (2014).
- 669 5 Gupta, H. S. *et al.* Cooperative deformation of mineral and collagen in bone at the  
670 nanoscale. *Proceedings of the National Academy of Sciences* **103**, 17741-17746  
671 (2006).
- 672 6 Tadano, S., Giri, B., Sato, T., Fujisaki, K. & Todoh, M. Estimating nanoscale  
673 deformation in bone by X-ray diffraction imaging method. *Journal of biomechanics*  
674 **41**, 945-952 (2008).
- 675 7 Orgel, J. P., Irving, T. C., Miller, A. & Wess, T. J. Microfibrillar structure of type I  
676 collagen in situ. *Proceedings of the National Academy of Sciences* **103**, 9001-9005  
677 (2006).
- 678 8 Gautieri, A., Vesentini, S., Redaelli, A. & Buehler, M. J. Hierarchical structure and  
679 nanomechanics of collagen microfibrils from the atomistic scale up. *Nano letters* **11**,  
680 757-766 (2011).
- 681 9 Dierolf, M. *et al.* Ptychographic X-ray computed tomography at the nanoscale. *Nature*  
682 **467**, 436-439 (2010).
- 683 10 Giannuzzi, L. A., Phifer, D., Giannuzzi, N. J. & Capuano, M. J. Two-dimensional and  
684 3-dimensional analysis of bone/dental implant interfaces with the use of focused ion  
685 beam and electron microscopy. *Journal of Oral and Maxillofacial Surgery* **65**, 737-  
686 747 (2007).
- 687 11 Schneider, P., Meier, M., Wepf, R. & Müller, R. Serial FIB/SEM imaging for  
688 quantitative 3D assessment of the osteocyte lacuno-canalicular network. *Bone* **49**,  
689 304-311 (2011).
- 690 12 Boyde, A. & Jones, S. J. Scanning electron microscopy of bone: instrument,  
691 specimen, and issues. *Microscopy research and technique* **33**, 92-120 (1996).
- 692 13 Song, M. J., Dean, D. & Tate, M. L. K. In situ spatiotemporal mapping of flow fields  
693 around seeded stem cells at the subcellular length scale. *PLoS one* **5**, e12796 (2010).

- 694 14 Roeder, B. A., Kokini, K., Robinson, J. P. & Voytik-Harbin, S. L. Local, three-  
695 dimensional strain measurements within largely deformed extracellular matrix  
696 constructs. *Journal of biomechanical engineering* **126**, 699-708 (2004).
- 697 15 Sztefek, P. *et al.* Using digital image correlation to determine bone surface strains  
698 during loading and after adaptation of the mouse tibia. *Journal of biomechanics* **43**,  
699 599-605 (2010).
- 700 16 Hoc, T. *et al.* Effect of microstructure on the mechanical properties of Haversian  
701 cortical bone. *Bone* **38**, 466-474 (2006).
- 702 17 Bay, B. K. Texture correlation: a method for the measurement of detailed strain  
703 distributions within trabecular bone. *Journal of Orthopaedic Research* **13**, 258-267  
704 (1995).
- 705 18 Nicoletta, D. P., Moravits, D. E., Gale, A. M., Bonewald, L. F. & Lankford, J.  
706 Osteocyte lacunae tissue strain in cortical bone. *Journal of biomechanics* **39**, 1735-  
707 1743 (2006).
- 708 19 Katsamenis, O. L., Chong, H. M., Andriotis, O. G. & Thurner, P. J. Load-bearing in  
709 cortical bone microstructure: Selective stiffening and heterogeneous strain  
710 distribution at the lamellar level. *Journal of the mechanical behavior of biomedical*  
711 *materials* **17**, 152-165 (2013).
- 712 20 Tai, K., Dao, M., Suresh, S., Palazoglu, A. & Ortiz, C. Nanoscale heterogeneity  
713 promotes energy dissipation in bone. *Nature materials* **6**, 454-462 (2007).
- 714 21 Hassenkam, T. *et al.* High-resolution AFM imaging of intact and fractured trabecular  
715 bone. *Bone* **35**, 4-10 (2004).
- 716 22 Thurner, P. J. *et al.* Imaging of bone ultrastructure using atomic force microscopy.  
717 *Modern research and educational topics in microscopy*, 37-48 (2007).
- 718 23 Pan, B. & Wang, B. A flexible and accurate digital volume correlation method  
719 applicable to high-resolution volumetric images. *Measurement Science and*  
720 *Technology* **28**, 105007 (2017).
- 721 24 Hussein, A. I., Barbone, P. E. & Morgan, E. F. Digital volume correlation for study of  
722 the mechanics of whole bones. *Procedia IUTAM* **4**, 116-125 (2012).
- 723 25 Bay, B. K., Smith, T. S., Fyhrie, D. P. & Saad, M. Digital volume correlation: three-  
724 dimensional strain mapping using X-ray tomography. *Experimental mechanics* **39**,  
725 217-226 (1999).
- 726 26 Roberts, B. C., Perilli, E. & Reynolds, K. J. Application of the digital volume  
727 correlation technique for the measurement of displacement and strain fields in bone: a  
728 literature review. *Journal of biomechanics* **47**, 923-934 (2014).
- 729 27 Barth, H. D., Launey, M. E., MacDowell, A. A., Ager III, J. W. & Ritchie, R. O. On  
730 the effect of X-ray irradiation on the deformation and fracture behavior of human  
731 cortical bone. *Bone* **46**, 1475-1485 (2010).
- 732 28 Currey, J. D. *et al.* Effects of ionizing radiation on the mechanical properties of  
733 human bone. *Journal of Orthopaedic Research* **15**, 111-117 (1997).
- 734 29 Staines, K. A., Poulet, B., Wentworth, D. N. & Pitsillides, A. A. The STR/ort mouse  
735 model of spontaneous osteoarthritis—an update. *Osteoarthritis and cartilage* **25**, 802-  
736 808 (2017).
- 737 30 De Fanis, A., Pešić, Z., Wagner, U. & Rau, C. Fast X-ray imaging at beamline I13L at  
738 Diamond Light Source. *Journal of Physics: Conference Series* **425**, 192014 (2013).
- 739 31 Karagadde, S. *et al.* Transgranular liquation cracking of grains in the semi-solid state.  
740 *Nature communications* **6**, 8300 (2015).
- 741 32 Kareh, K., Lee, P., Atwood, R., Connolley, T. & Gourlay, C. Revealing the  
742 micromechanisms behind semi-solid metal deformation with time-resolved X-ray  
743 tomography. *Nature communications* **5**, 4464 (2014).

- 744 33 Bay, B. K. Methods and applications of digital volume correlation. *The Journal of*  
745 *Strain Analysis for Engineering Design* **43**, 745-760 (2008).
- 746 34 De Souza, R. L. *et al.* Non-invasive axial loading of mouse tibiae increases cortical  
747 bone formation and modifies trabecular organization: a new model to study cortical  
748 and cancellous compartments in a single loaded element. *Bone* **37**, 810-818 (2005).
- 749 35 Goldring, M. B. & Goldring, S. R. Articular cartilage and subchondral bone in the  
750 pathogenesis of osteoarthritis. *Annals of the New York Academy of Sciences* **1192**,  
751 230-237 (2010).
- 752 36 Lories, R. J. & Luyten, F. P. The bone–cartilage unit in osteoarthritis. *Nature Reviews*  
753 *Rheumatology* **7**, 43-49 (2011).
- 754 37 Müller, R. Hierarchical microimaging of bone structure and function. *Nature Reviews*  
755 *Rheumatology* **5**, 373-381 (2009).
- 756 38 Yamada, S., Tadano, S. & Fujisaki, K. Residual stress distribution in rabbit limb  
757 bones. *Journal of biomechanics* **44**, 1285-1290 (2011).
- 758 39 Gupta, H. S. *et al.* Nanoscale deformation mechanisms in bone. *Nano letters* **5**, 2108-  
759 2111 (2005).
- 760 40 Campbell, S. E., Ferguson, V. L. & Hurley, D. C. Nanomechanical mapping of the  
761 osteochondral interface with contact resonance force microscopy and  
762 nanoindentation. *Acta biomaterialia* **8**, 4389-4396 (2012).
- 763 41 Mente, P. & Lewis, J. L. Elastic modulus of calcified cartilage is an order of  
764 magnitude less than that of subchondral bone. *Journal of Orthopaedic Research* **12**,  
765 637-647 (1994).
- 766 42 Hargrave-Thomas, E., van Sloun, F., Dickinson, M., Broom, N. & Thambyah, A.  
767 Multi-scalar mechanical testing of the calcified cartilage and subchondral bone  
768 comparing healthy vs early degenerative states. *Osteoarthritis and cartilage* **23**, 1755-  
769 1762 (2015).
- 770 43 Doube, M., Firth, E. & Boyde, A. Variations in articular calcified cartilage by site and  
771 exercise in the 18-month-old equine distal metacarpal condyle. *Osteoarthritis and*  
772 *cartilage* **15**, 1283-1292 (2007).
- 773 44 Day, J. *et al.* Adaptation of subchondral bone in osteoarthritis. *Biorheology* **41**, 359-  
774 368 (2004).
- 775 45 Li, B. & Aspden, R. M. Mechanical and material properties of the subchondral bone  
776 plate from the femoral head of patients with osteoarthritis or osteoporosis. *Annals of*  
777 *the Rheumatic Diseases* **56**, 247-254 (1997).
- 778 46 Li, B. & Aspden, R. M. Composition and mechanical properties of cancellous bone  
779 from the femoral head of patients with osteoporosis or osteoarthritis. *Journal of Bone*  
780 *and Mineral Research* **12**, 641-651 (1997).
- 781 47 Jaiprakash, A. *et al.* Phenotypic characterization of osteoarthritic osteocytes from the  
782 sclerotic zones: a possible pathological role in subchondral bone sclerosis.  
783 *International journal of biological sciences* **8**, 406-417 (2012).
- 784 48 Couchourel, D. *et al.* Altered mineralization of human osteoarthritic osteoblasts is  
785 attributable to abnormal type I collagen production. *Arthritis & Rheumatism* **60**, 1438-  
786 1450 (2009).
- 787 49 Poulet, B. *et al.* Intermittent applied mechanical loading induces subchondral bone  
788 thickening that may be intensified locally by contiguous articular cartilage lesions.  
789 *Osteoarthritis and cartilage* **23**, 940-948 (2015).
- 790 50 Van Ruijven, L., Mulder, L. & Van Eijden, T. Variations in mineralization affect the  
791 stress and strain distributions in cortical and trabecular bone. *Journal of biomechanics*  
792 **40**, 1211-1218 (2007).

- 793 51 Mori, S., Harruff, R. & Burr, D. Microcracks in articular calcified cartilage of human  
794 femoral heads. *Archives of pathology & laboratory medicine* **117**, 196-198 (1993).
- 795 52 Pan, J. *et al.* Elevated cross-talk between subchondral bone and cartilage in  
796 osteoarthritic joints. *Bone* **51**, 212-217 (2012).
- 797 53 Suri, S. & Walsh, D. A. Osteochondral alterations in osteoarthritis. *Bone* **51**, 204-211  
798 (2012).
- 799 54 Pouran, B. *et al.* Solute transport at the interface of cartilage and subchondral bone  
800 plate: effect of micro-architecture. *Journal of biomechanics* **52**, 148-154 (2017).
- 801 55 Muir, P. *et al.* Role of endochondral ossification of articular cartilage and functional  
802 adaptation of the subchondral plate in the development of fatigue microcracking of  
803 joints. *Bone* **38**, 342-349 (2006).
- 804 56 Laverty, S., Lacourt, M., Gao, C., Henderson, J. & Boyde, A. High density infill in  
805 cracks and protrusions from the articular calcified cartilage in osteoarthritis in  
806 standardbred horse carpal bones. *International journal of molecular sciences* **16**,  
807 9600-9611 (2015).
- 808 57 Boyde, A. *et al.* On fragmenting, densely mineralised acellular protrusions into  
809 articular cartilage and their possible role in osteoarthritis. *Journal of anatomy* **225**,  
810 436-446 (2014).
- 811 58 Turley, S. M., Thambyah, A., Riggs, C. M., Firth, E. C. & Broom, N. D.  
812 Microstructural changes in cartilage and bone related to repetitive overloading in an  
813 equine athlete model. *Journal of anatomy* **224**, 647-658 (2014).
- 814 59 Boyde, A. *et al.* Cartilage damage involving extrusion of mineralisable matrix from  
815 the articular calcified cartilage and subchondral bone. *Eur Cell Mater* **21**, 470-478  
816 (2011).
- 817 60 Boyde, A. The real response of bone to exercise. *Journal of anatomy* **203**, 173-189  
818 (2003).
- 819 61 Comhaire, F. H. & Snaps, F. Comparison of two canine registry databases on the  
820 prevalence of hip dysplasia by breed and the relationship of dysplasia with body  
821 weight and height. *American journal of veterinary research* **69**, 330-333 (2008).
- 822 62 Staines, K., Pollard, A., McGonnell, I., Farquharson, C. & Pitsillides, A. Cartilage to  
823 bone transitions in health and disease. *The Journal of endocrinology* **219**, R1-R12  
824 (2013).
- 825 63 Staines, K. *et al.* Endochondral growth defect and deployment of transient  
826 chondrocyte behaviors underlie osteoarthritis onset in a natural murine model.  
827 *Arthritis & Rheumatology* **68**, 880-891 (2016).
- 828 64 Pitsillides, A. A. & Beier, F. Cartilage biology in osteoarthritis—lessons from  
829 developmental biology. *Nature Reviews Rheumatology* **7**, 654-663 (2011).
- 830 65 Puncreobutr, C., Lee, P., Hamilton, R. & Phillion, A. Quantitative 3D characterization  
831 of solidification structure and defect evolution in Al alloys. *Jom* **64**, 89-95 (2012).
- 832 66 Maksimcuka, J. *et al.* X-ray tomographic imaging of tensile deformation modes of  
833 electrospun biodegradable polyester fibers. *Frontiers in Materials* **4**, 43 (2017).
- 834 67 Poulet, B., Hamilton, R. W., Shefelbine, S. & Pitsillides, A. A. Characterizing a novel  
835 and adjustable noninvasive murine joint loading model. *Arthritis & Rheumatism* **63**,  
836 137-147 (2011).
- 837 68 Nazarian, A., Stauber, M., Zurakowski, D., Snyder, B. D. & Müller, R. The  
838 interaction of microstructure and volume fraction in predicting failure in cancellous  
839 bone. *Bone* **39**, 1196-1202 (2006).
- 840 69 Rau, C., Wagner, U., Pešić, Z. & De Fanis, A. Coherent imaging at the Diamond  
841 beamline I13. *physica status solidi (a)* **208**, 2522-2525 (2011).

842 70 Pešić, Z., De Fanis, A., Wagner, U. & Rau, C. Experimental stations at I13 beamline  
843 at Diamond Light Source. *Journal of Physics: Conference Series* **425**, 182003 (2013).  
844 71 Christen, D. *et al.* Deformable image registration and 3D strain mapping for the  
845 quantitative assessment of cortical bone microdamage. *Journal of the mechanical*  
846 *behavior of biomedical materials* **8**, 184-193 (2012).  
847 72 Voide, R. *et al.* Time-lapsed assessment of microcrack initiation and propagation in  
848 murine cortical bone at submicrometer resolution. *Bone* **45**, 164-173 (2009).  
849 73 Pacureanu, A., Langer, M., Boller, E., Tafforeau, P. & Peyrin, F. Nanoscale imaging  
850 of the bone cell network with synchrotron X-ray tomography: optimization of  
851 acquisition setup. *Medical physics* **39**, 2229-2238 (2012).  
852 74 Basham, M. *et al.* Data analysis workbench (DAWN). *Journal of synchrotron*  
853 *radiation* **22**, 853-858 (2015).  
854 75 Titarenko, V. Analytical formula for two-dimensional ring artefact suppression.  
855 *Journal of synchrotron radiation* **23**, 1447-1461 (2016).  
856 76 Madi, K. *et al.* Computation of full-field displacements in a scaffold implant using  
857 digital volume correlation and finite element analysis. *Medical engineering & physics*  
858 **35**, 1298-1312 (2013).  
859 77 Abd-Elmoniem, K. Z., Stuber, M. & Prince, J. L. Direct three-dimensional  
860 myocardial strain tensor quantification and tracking using zHARP. *Medical image*  
861 *analysis* **12**, 778-786 (2008).  
862